ELSEVIER

Molecular-level design of isolated molybdenum oxide anchored on carbon nitride for photocatalytic H$_2$ production and environmental remediation

Milad Jourshabani , Mahdieh Razi Asrami , Byeong-Kyu Lee [*]

Department of Civil and Environment Engineering, University of Ulsan, Daehakro 93, Namgu, Ulsan 44610, Republic of Korea

ABSTRACT

Polymeric carbon nitride typically suffers from sluggish intrinsic charge separation and low available active sites. This paper reports that isolated non-crystalline molybdenum oxide species anchored to N-coordinating cavities (MoCN) have abundant surface-active sites for solid–liquid two-phase reactions, whether for photocatalytic H$_2$ evolution or organic pollutant degradation. Molecular dynamic simulations and density functional theory (DFT) revealed six-fold cavities to stabilize the MoO$_3$ species with non-crystalline features, endowing high dispersion and less aggregation. As proven in single-site heterogeneous catalysts, the photocatalyst benefits from size reduction and accelerated interfacial charge transfer because of its mutual contact between two semiconductors. The MoCN shows a high visible-light H$_2$ evolution of 1265 μmol g^{-1}h^{-1} under visible light ($\lambda \geq$ 400 nm) illumination. The photocatalyst degraded more than 95% tetracycline within 30 min and rhodamine B in 10 min. The MoO$_3$ species confined within π-conjugated systems increase the catalytic contact sites, extending visible light harvesting ability to a longer wavelength. Each single catalytic site facilitates the separation and transfer of charge carriers while interfacial charge still occurs between MoO$_3$ and CN. This molecular-level design and strategy provide a new opportunity and a universal way to extend the boundaries of liquid–solid phase catalysts.

1. Introduction

Solar light is an almost free and inexhaustible energy resource, but its ultraviolet (UV) fraction is limited to 3–5%, which is one of the significant drawbacks to conventional photocatalysis using UV-active TiO$_2$ [1]. The visible-light-active photocatalysis with a large response to the whole sunlight spectrum is the key to the practical applications to energy and environmental issues. Polymeric carbon nitride (CN) is considered a visible-light-active photocatalyst with many merits, including adjustable electronic units of π-conjugated heptazine units, environmental benignity, and high thermal and chemical stability [1]. Moreover, CN can be fabricated easily by the thermal polycondensation of cheap nitrogen-rich precursors [2–4]. Nevertheless, traditional polycondensation leads to CN with less condensed heptazine units because the solid-state reaction is limited by the immobility of intermediates and their sublimation during the heating process [5]. This deficiency leads to bulk CN exhibiting poor visible-near infrared (NIR) light harvesting, rapid electron–hole recombination, and a low specific surface area [6].

Supramolecular chemistry can solve this issue by forming a preorganized state of precursors, endowing new physicochemical properties to the starting materials [5,7]. Shalom et al. reported that the thermal polycondensation of a cyanuric acid–melamine (CM) complex led to either templated growth or topotactic transformation and provided CN with a highly condensed structure [8]. On the other hand, some inherent characteristics remain, which include the weak oxidation ability of CN owing to less positive valance band (VB) potential compared with some half-reactions, such as OH$^-$/•OH (1.99 eV vs. NHE) [9].

As a second solution, rationally designing a heterojunction between the modified CN with another semiconductor has become a research hotspot because, in heterojunction systems, the redox ability can be reached to a great level via a direct Z-scheme charge transfer mechanism [10–12]. For example, it has been proven that MoO$_3$ is a promising semiconductor owing to environmental friendliness, visible-light activity, low cost, and its well-matched band alignment with CN for constructing a Z-scheme pathway [13]. Nevertheless, the fabrication of heterojunctions is challenging because an efficient and intimate solid–solid contact interface with high homodispersion is often affected by the synthesis conditions [10]. Consider MoO$_3$ particles sparsely
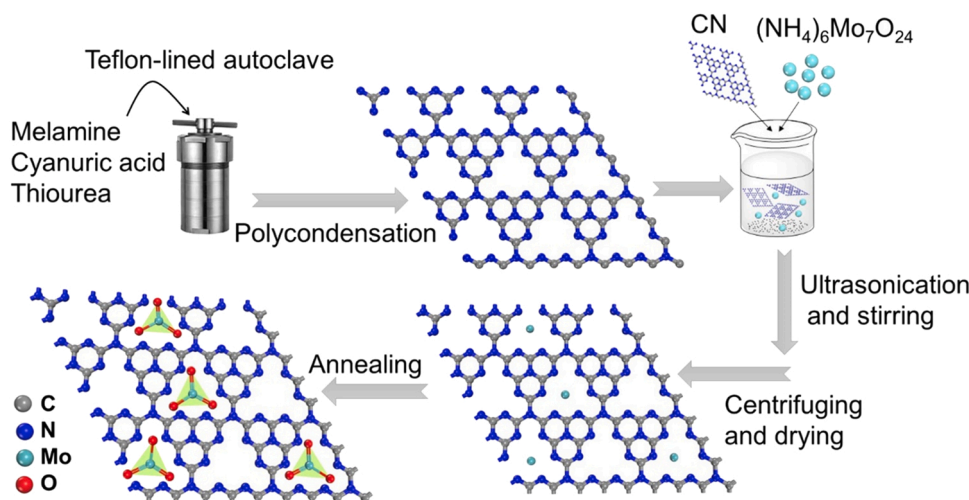
---

* Corresponding author.
 E-mail address: bklee@ulsan.ac.kr (B.-K. Lee).

Scheme 1. Schematic illustration of the formation of non-crystalline MoO_3 anchored on carbon nitride (3.8-MoCN).

dispersed on the surface of CN. Small solid–solid contact can be formed, which is insufficient to transfer photogenerated electrons effectively between two counterparts. In addition, overloading MoO_3 from the optimal mass value results in the confinement effect that causes less penetration of incident light into the CN surface, leading to fewer photogenerated electron–hole pairs. Recently, a $MoO_3/g\text{-}C_3N_4$ Z-scheme heterojunction was prepared by the physical mixing of MoO_3 nanoparticles and $g\text{-}C_3N_4$ followed by calcination [13]. The material showed the highest photocatalytic activity of 85.9% within 100 min for the degradation of tetracycline was obtained when the mass fraction of MoO_3 was 0.5. On the other hand, its photocatalytic efficiency per gram of composite is still low. The high homodispersion of MoO_3 on the CN surface effectively increases the contact area and active surface sites. The ultimate frontier in homodispersion is single-site atom catalysts [14]. Nevertheless, single-site molybdenum cannot act as a semiconductor, and fewer charge carriers can be expected from just one semiconductor [15].

Inspired by heterojunctions and single-site catalyst characteristics, the highest photocatalytic activity might be obtained by anchoring noncrystalline MoO_3 species to the N-coordinating cavities. CN can provide isolated and highly stable form of non-crystalline MoO_3 species and prevent the thermodynamic instability of MoO_3 species by six-fold cavities while assuring its semiconductor properties. Unfortunately, less attention has been paid to the six-fold cavities of CN to stabilize metal oxide species, endowing new opportunities for constructing photocatalysis materials.

This paper reports the controllable non-crystalline MoO_3 anchored on N-coordinating cavities of highly condensed carbon nitride (3.8-MoCN) for the first time. This isolated 3.8-MoCN photocatalyst exhibited many advantages because it comprises a homodispersion of MoO_3 species within N-coordinating six-fold cavities, which is similar to a single-site atom, preventing the aggregation of MoO_3 nanoparticles as demonstrated by density functional theory (DFT) calculations. In addition, the photocatalyst would obey a direct Z-scheme feature in which charge carriers with the strongest redox ability are formed. Moreover, we prepared a heterojunction from the high crystalline MoO_3 deposited on a CN surface (cry-MoCN) for accurate comparison. The photocatalytic activity for two well-known solid–liquid reactions, including H_2 evolution and organic pollutant degradation, was investigated under visible-light irradiation. Tetracycline fragmentation and its degradation intermediates were evaluated by liquid chromatography–tandem mass spectrometry (LC–MS/MS). The toxicity of the intermediates and possible photocatalytic mechanisms are also discussed in detail.

2. Materials and methods

2.1. Chemicals

Melamine, isopropyl alcohol (IPA), benzoquinone (BQ), cyanuric acid, thiourea, triethanolamine (TEOA), rhodamine B (RhB), terephthalic acid (TA), and ammonium molybdate tetrahydrate were purchased from Daejung Chemicals & Metals Co. Ltd. (Gyeonggi‐Do, Korea). Tetracycline (TC) was obtained from Sigma‐Aldrich Co. All chemicals were of analytical grade and used as received. Distilled water was used as the solvent for all the experiments.

2.2. Synthesis of CN

The polycondensation process of a preorganized supramolecular complex leads to carbon nitride structures with improved condensed structures, charge separation, and electronic conductivities [8]. A preorganized supramolecular complex was prepared by mixing cyanuric acid, thiourea, and melamine with a 2:2:2 mass ratio. First, each precursor was dispersed separately in 60 mL of boiling water to form translucent suspensions. The three solutions were transferred to a Teflon-lined stainless-steel autoclave and maintained at 100 °C for 4 h. After natural cooling to room temperature, the precipitates were centrifuged and dried overnight in an oven at 80 °C. The resulting solids were powdered in an agate mortar to obtain a self-assembly complex.

The self-assembly powder (2.5 g) was placed in a crucible with a lid and annealed at 540 °C for 3 h under a N_2 atmosphere at a heating rate of 3.0 °C min^{-1} to give highly condensed CN. For comparison, bulk carbon nitride (BCN) was prepared using only melamine as a precursor. The melamine was calcined at 540 °C for 3 h in air at a heating rate of 3.0 °C min^{-1}.

2.3. Synthesis of non-crystalline MoO_3 anchored on CN (3.8-MoCN)

The CN powder (0.8 g) was mixed in 100 mL of water and then sonicated for 1 h to disperse the CN sheets. A certain amount of ammonium molybdate tetrahydrate (0.005, 0.010, and 0.200 g) was added to the suspension of CN with vigorous stirring for 15 min. The procedure was followed by ultrasonication for 1 h to obtain well‐dispersed metal ions within the CN particles. Subsequently, the suspension was mixed under magnetic stirring overnight at room temperature to stabilize the metal ions adsorbed on the N-coordinating six-fold cavities of CN. The resulting solid was centrifuged and washed several times with water to remove the unstable molybdenum ions from the CN surface. After drying at 80 °C for 24 h, the solid material was gathered in

a mortar to obtain homogeneity. The powder was loaded into a crucible with a lid and annealed at 540 °C for 3 h at a heating ramp of 3.0 °C min^{-1} in air. The molybdenum ions adsorbed on the N-coordinating cavities of CN started to oxidize in air to give non-crystalline MoO_3 anchored on CN (x-MoCN, x represents the mass fraction of MoO_3). Harsh reaction conditions, such as high temperature or semi-open crucible, can convert molybdenum species to MoO_3 nanoparticles, which are deposited on the CN sheets. Because 3.8 wt% MoCN (3.8-MoCN) showed the highest photocatalytic performance, it was chosen as a representative sample in the subsequent experiments.

For comparison, a heterojunction of the crystalline MoO_3 nanoparticles deposited on the CN sheets was prepared and called cry-MoCN. All synthesis processes were the same as 3.8-MoCN, except that the last heating step was conducted at 540 °C for 3 h at a heating ramp of 3.0 °C min^{-1} and then kept at this temperature for 1 h in air. To study the annealing effect, 3.8-MoCN photocatalyst was prepared in exactly the same condition as 3.8-MoCN without an annealing step (it is denoted as un-3.8-MoCN). A sample of MoO_3 nanoparticles was prepared exactly in the same temperature condition as 3.8-MoCN without using the CN photocatalyst (MoO_3). Scheme 1 presents a schematic diagram of the synthesis pathway of 3.8-MoCN as a target photocatalyst.

2.4. Characterization

Field‐emission scanning electron microscopy (SEM, FEI Nova NanoSEM) images were taken using a Schottky‐type thermal FE gun operating at 15 kV. Transmission electron microscopy (TEM, JEOL, JEM‐2100 F) was performed at an acceleration voltage of 200 kV. X-ray photoelectron spectroscopy (XPS, ESCALAB 250XI, Thermo Fisher Scientific) was conducted using a monochromated Al–Kα source with an energy step size of 1.0 eV under an ultrahigh vacuum of $1.0 \times 10^{r-f10}$ Torr. Fourier transform infrared (FT-IR, Varian, Model-670/620) spectra were recorded from KBr pellet samples in the range 4000–400 cm^{-1}. Thermogravimetric analysis (TGA) was performed on a Q500 apparatus. Nitrogen adsorption–desorption isotherms were measured on a Micromeritics Instruments, ASAP2020 instrument. All samples were degassed at 150 °C for 3 h before the measurements. The specific surface area and the pore size distributions were extracted from the Brunauer–Emmett–Teller (BET) and Barrett–Joyner–Halenda (BJH) equations, respectively. X-ray diffraction (XRD Bruker, D8 ADVANCE) was conducted using monochromatic Cu–Kα radiation ($\lambda = 1.5418$ Å), ranging from 10° to 80° 2θ. Electron paramagnetic resonance (EPR) measurements in the X-band (9.64 GHz) were performed using a CW/Pulse EPR System(QM09). A time-resolved fluorescence lifetime study was carried out using a confocal microscope (MicroTime-200, Picoquant, Germany) with a 40 × objective. A single-mode pulsed diode laser (375 nm with 30 ps pulse width and an average laser power of ~3 nW) was used as the excitation source. A dichroic mirror (Z375RDC, AHF), a longpass filter (HQ405lp, AHF), a 100 μm pinhole, and an avalanche photodiode detector (PDM series, MPD) were used to collect the emission photons from the samples. The photoluminescence (PL) spectra were carried out using an Edinburgh Instrument NF900 (FLS920) spectrophotometer. Liquid chromatography–tandem mass spectrometry (LC–MS/MS) was conducted using a 1200 Series & HCT basic system from 50 to 3000 m/z. UV-Vis diffuse reflectance spectra (DRS) were carried out using Agilent, Cary 5000 spectrophotometry. The band gap was calculated according to Kubelka–Munk theory (Eq. (1)) and using the Tauc plot, i.e., (F(R)hν)^n against (hν). F(R), R$_\infty$, h, and ν are the Kubelka–Munk function, the reflectance of a layer, the Planck constant, and the frequency of radiation, respectively. The bandgap (E$_g$) was estimated from an extrapolation of the linear section of the spectra to the hν axis.

$$\frac{(1-R)^2}{2 \times R_\infty} = F(R) \quad (1)$$

2.5. Computational details

DFT calculations were used to investigate the geometric and electronic properties of 3.8-MoCN structures in different positions. The calculations were carried out by applying the Perdew–Burke–Ernzerhof (PBE) function within the generalized gradient approximation (GGA). A vacuum space of 20 Å in the z-direction for each structure was used to avoid the interaction between layers. Moreover, no constraint was imposed for atoms during the geometry optimization. In order to reach accurate results, the cutoff energy was set to 450 eV and Brillouin-zone with a $2 \times 2 \times 3$ k-point grid. Geometry relaxations were performed until they reached the maximum force of 0.05 eV/Å and the maximum displacement of 0.02 Å, while energy was set to be smaller than 2.0×10^{-5} eV/atom.

The annealing effect on the behavior of the Mo/CN photocatalyst during the synthesis process was analyzed using molecular dynamics simulation. At first, the 3.8-MoCN was optimized, and the system was heated up from 25 to 550°C. The simulation was taken at 10 ps, with a time step of 2 fs and heating ramps per cycle of 500, while the total steps were 5000.

2.6. Electrochemical measurements

Electrochemical impedance spectroscopy (EIS) and transient photocurrent response of the photocatalysts were monitored using a Versa STAT, Princeton Applied Research system with a conventional three-electrode cell. The working electrodes were fabricated by coating a slurry of the as-prepared photocatalyst on a 2.5 cm × 2.5 cm fluorine doped tin oxide (FTO) substrate using a spin coating technique followed by heating at 250 °C for 1 h in air. The slurry was prepared as follows: 5 mg of the photocatalyst was dispersed to 1 mL of ethanol, followed by the addition of 30 μL of a Nafion solution (5.0 wt%). The mixture was sonicated for 30 min to give a homogenized suspension. The working electrode was immersed in 0.5 M Na_2SO_4 aqueous solution with a Ag/AgCl electrode (saturated KCl solution) and Pt wire as the reference and counter electrodes, respectively. The EIS curve was conducted at the amplitude of 5 mV and frequency range of 0.1–10^5 Hz. All results vs. Ag/AgCl were converted to the reversible hydrogen electrode (RHE) using the Nernst equation at room temperature, according to Eq. (2):

$$E_{RHE} = E_{AgCl} + E^0_{AgCl} + 0.059PH \quad (2)$$

2.7. Photocatalytic activity tests

The performance of the photocatalyst was investigated by the photocatalytic degradation of RhB as a typical reference. The efficiency was assessed further through the degradation of TC as an emerging pharmaceutical pollutant. In a typical reaction, 10 mg of catalyst was dispersed ultrasonically in 15 mL of RhB solution (12 mg L^{-1}) or TC solution (20 mg L^{-1}). After reaching absorption–desorption equilibrium in the dark for 60 min, a Pyrex vial was placed in front of the light source provided by a 300 W Xe lamp with a 400 nm cutoff filter. The light intensity was measured with a thermophile sensor (818 P-001–12, Newport) and was 395 mW cm^{-2}. At a certain time interval, 2.5 mL of the sample was taken and centrifuged for the UV–vis spectrophotometry analysis. In the case of the TC solution, a 0.45 μm membrane filter was used to separate the photocatalyst.

The photocatalytic activity was calculated using Eq. (3), where η, C$_0$, and C$_t$ are the photocatalytic efficiency, initial concentration, and concentration after the illumination time, respectively. Furthermore, the degradation evaluation was well fitted to the Langmuir-Hinshelwood (L–H) model, where pseudo-first order reaction kinetics was calculated using Eq. (4). η, C$_0$, and C$_t$ are the photocatalytic efficiency, the adsorption–desorption equilibrium concentration, and concentration at the reaction time, respectively.
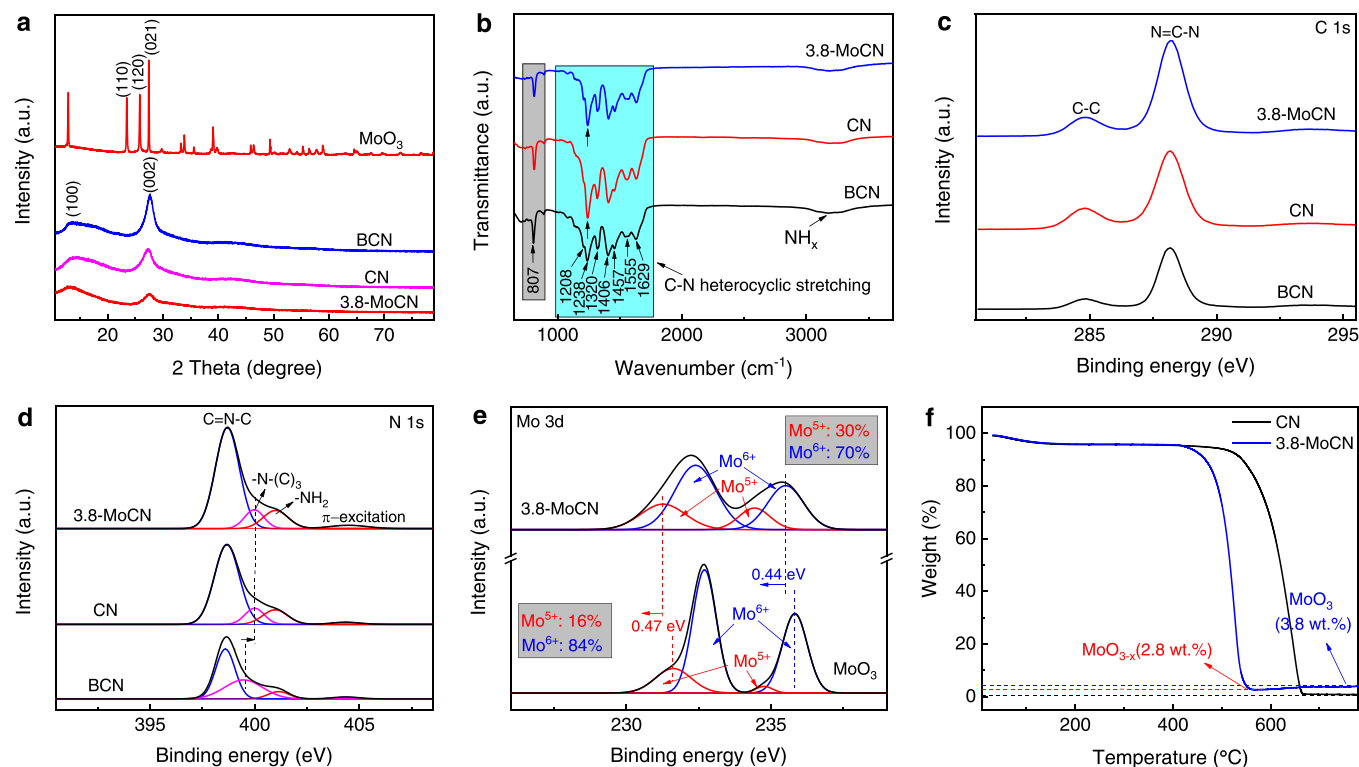
Fig. 1. (a) XRD patterns and (b) FT-IR spectra of BCN, CN, and 3.8-MoCN; high-resolution XPS spectra of (c) C 1s, (d) N 1s, and (e) Mo 3d; (f) TGA curve of CN and 3.8-MoCN.

The apparent quantum efficiency (AQE) of degradation of RhB was measured under the monochromated illumination at a wavelength of 380 nm, 400 nm, 420, 440, 460 nm and identical reaction conditions. The AQE was calculated according to Eqs. (5–8). Where N_A is the Avogadro constant, approximately 6.022×10^{23} mol^{-1}, n is the number of degraded RhB molecules, h (J.s) is Planck's constant, c (m s^{-1}) is the speed of light, P (W m^{-2}) is the power density of the incident monochromatic light, λ_{inc} (m) is the wavelength of the monochromatic light, t (s) is the duration of the incident light irradiation, and S is the irradiation area.

$$\eta = \frac{(C_0 - C_t)}{C_0} \quad (3)$$

$$\ln \frac{C_0}{C_t} = k_{app} \times t \quad (4)$$

$$AQE[\%] = \frac{Number\ of\ degraded\ RhB\ molecules}{Number\ of\ incident\ photons} \times 100 \quad (5)$$

$$Number\ of\ degraded\ pollutant\ molecules = N_A n_{RhB} \quad (6)$$

$$Number\ of\ incident\ photons = \frac{PS\lambda_{inc}t}{hc} \quad (7)$$

$$AQE\left[\%\right] = \frac{N_A n_{RhB} hc}{PS\lambda_{inc}t} \times 100 \quad (8)$$

2.8. Photocatalytic H₂ production

This study also investigated the prepared materials for photocatalytic H₂ production because this reaction is affected by active surface sites. A Pyrex front-irradiation reaction vail equipped with a gas ball valve was used under 300 W Xe-lamp with a cutoff filter ($\lambda \geq$ 400 nm). For each reaction, 5 mg of the photocatalyst was dispersed in 10 mL of an aqueous 20% triethanolamine by volume as a sacrificial reagent. A nominal 1 wt% Pt was photodeposited onto the surface of the photocatalysts by dissolving H₂PtCl₆ under 300 W Xe lamp irradiation for 60 min. Nitrogen was flowed through the reaction solution for half an hour before illumination assuring anaerobic conditions. Intermittently, 0.5 mL of gas was sampled through the valve. The evolved gases were analyzed by gas chromatography (Agilent 8890 A GC) equipped with a thermal conductive detector.

2.9. Detection of active species

A series of scavenging experiments were conducted by adding 100 mM IPA, BQ, and TEOA to the parent solution as the scavengers of hydroxyl radicals (•OH), superoxide radicals (•O₂⁻), and holes (h⁺), respectively, to recognize the generated active species in the degradation reaction. A PL technique was also utilized with terephthalic acid (TA) acting as the probe molecule to quantify the produced amount of •OH radicals in the photoreaction system. Indeed, TA has no fluorescent feature while it can react with •OH radicals to produce 2-hydroxyterephthalic acid with a strong fluorescent feature. Briefly, 10 mg of sample was added to 20 mL of TA solution (5 mM) containing 400 μL of NaOH 4 M. The solution was irradiated by a visible-light source for 5, 15, and 30 min. The photocatalyst was separated by centrifugation, and the supernatant was measured by PL analysis. The PL sharp peak around 450 nm, which was attributed to 2-hydroxyterephthalic acid, was monitored at an excitation wavelength of 315 nm [16].

3. Results and discussion

3.1. Chemical structure and morphology

Fig. 1a presents the XRD of 3.8-MoCN, CN, and BCN. The XRD patterns exhibit the reflections at 13.1° (100) and 27.4° (002) 2θ, which were assigned to in-plane repeating motifs of tri-s-triazine units and graphite-like interlayer stacking of the conjugated aromatic systems,

Table 1
Chemical states and atomic compositions for Mo 3d area.

Sample	Region	N–C=N /C–C	C–N=C /N– (C)$_3$	(at%)	BE (eV)	Oxidation state	Species
MoO$_3$	O 1 s	-	-	65.84	530.6	M=O	MoO$_{2.6}$
	Mo 3d$_{3/2}$, Mo 3d$_{5/2}$	-	-	24.97	232.7, 235.8	Mo^{6+} (84%)	
	Mo 3d$_{3/2}$, Mo 3d$_{5/2}$				231.6, 234.7	Mo^{5+} (16%)	
3.8-MoCN	O 1 s	5.80	6.50	0.24	530.6	M=O	MoO$_{2.4}$
	O 1 s	-	-	1.09	532.3	O-H or O adsorbed	-
	Mo 3d$_{3/2}$, Mo 3d$_{5/2}$	-	-	0.1	232.3, 235.5	Mo^{6+} (70%)	-
	Mo 3d$_{3/2}$, Mo 3d$_{5/2}$	-	-		231.2, 234.4	Mo^{5+} (30%)	-
CN	-	4.27	6.50	-	-	-	-
BCN	-	2.03	1.21	-	-	-	-

respectively [17]. In addition, the XRD peak at 27.4° 2θ for 3.8-MoCN become weaker than that of CN and BCN, indicating a decrease in the stacking layers along the c-axis [18]. These structural changes help increase the surface area and photocatalytic activity. From Fig. 1a, the common XRD reflections of MoO$_3$ were observed at 23.4°, 25.7°, and 27.5° 2θ, which represent the crystal planes of the (110), (120), and (021), respectively [13]. Furthermore, no XRD peaks for MoO$_3$ particles were observed in the case of the 3.8-MoCN photocatalyst, suggesting non-crystalline MoO$_3$ anchored to the N-coordinating six-fold cavities of the CN surface. Therefore, MoO$_3$ can be formed in host cavities, making a new design of the stable isolated form of the heterogeneous photocatalyst with minimum aggregation.

FT-IR spectroscopy confirmed the presence of highly condensed heptazine aromatic segments in all samples (Fig. 1b). The absorption band at 807 cm^{-1} was assigned to the out-of-plane vibrations of the tri-*s*-triazine ring. In contrast, the bands at 1208, 1238, 1320, 1406, 1457, 1555, and 1629 cm^{-1} were attributed to the aromatic heterocyclic stretching [19]. The broad band at 3000–3400 cm^{-1} was related to the uncondensed terminal NH$_x$ stretching [3]. Comparatively, the stretching vibration mode for 3.8-MoCN and CN at 1238 cm^{-1} became more pronounced than in BCN, indicating that more heptazine units were obtained.

XPS was conducted to examine the surface chemical states and composition of all samples. Fig. 1c presents the C 1s spectra of 3.8-MoCN, CN, and BCN. Two prominent peaks at 284.8 eV and 288.2 eV correspond to adventitious carbon C–C and N–C=N bonds, respectively [20]. For the N 1s spectrum of BCN, three peaks at 398.7, 399.6, and 400.9 eV were fitted, which were attributed to the C–N=C (sp^2), N–C$_3$ (sp^3), and –NH$_x$ pending group (Fig. 1d), respectively [21]. In addition, a small peak at 404.4 eV is related to the π-excitation of C–N
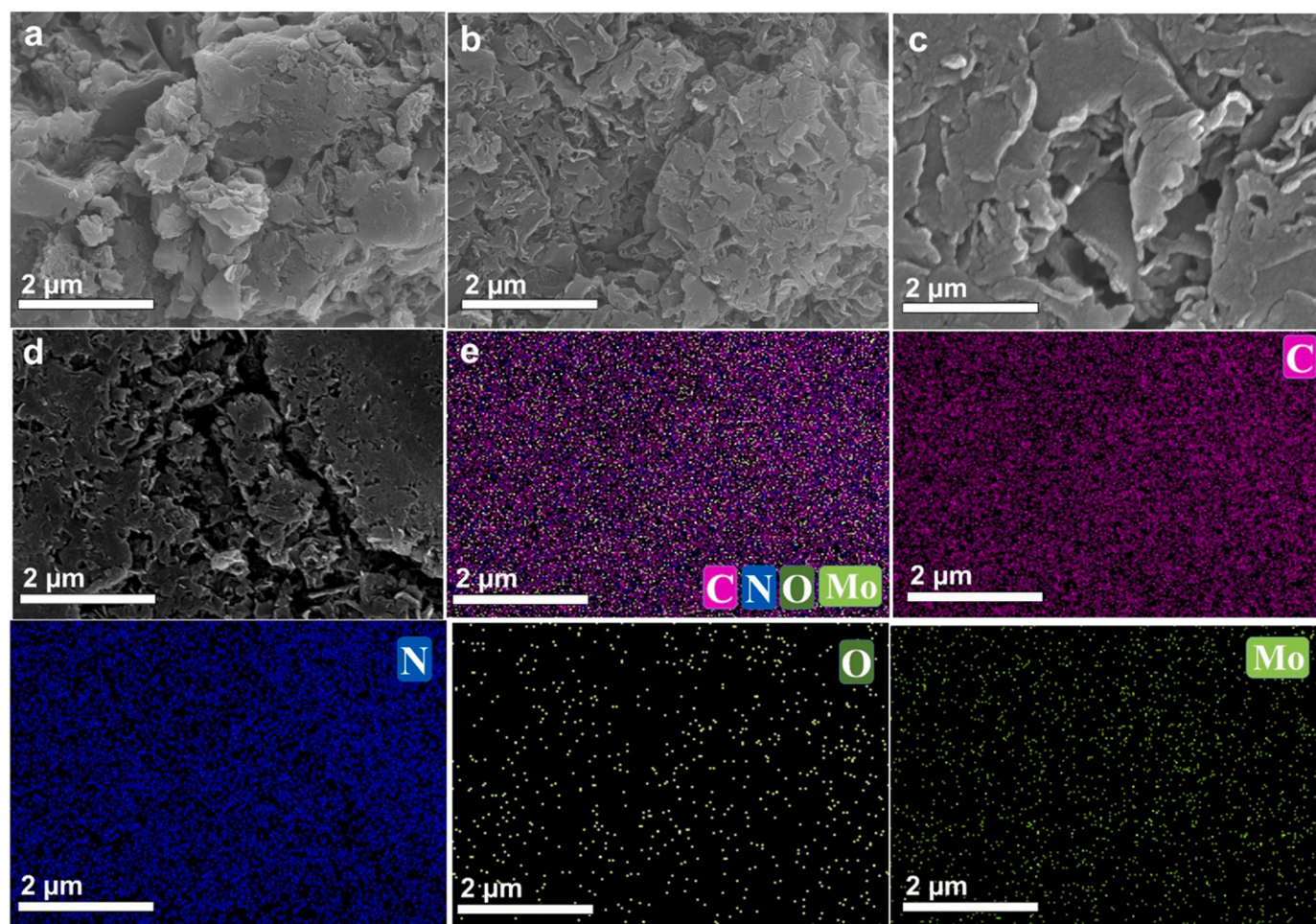

Fig. 2. FE-SEM images of (a) BCN, (b) CN, and (c) 3.8-MoCN; (d and e) EDS maps of 3.8-MoCN along with the distribution of C, N, O, and Mo.
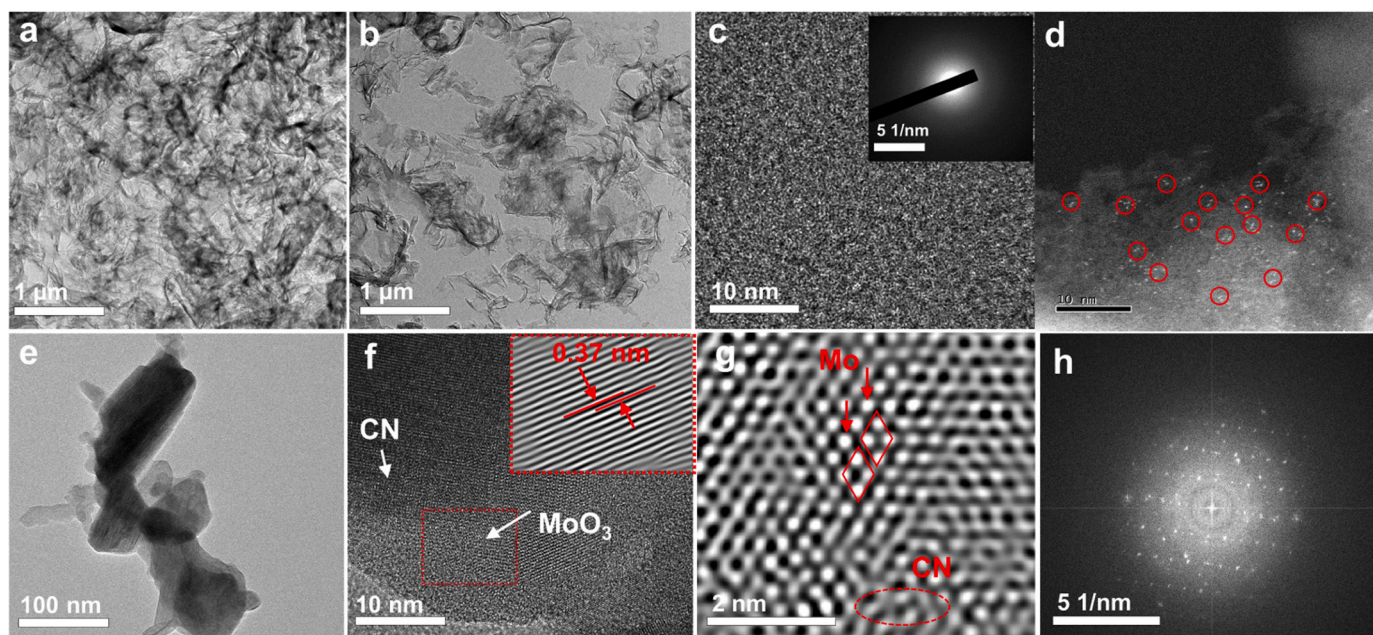
Fig. 3. TEM images of (a) CN and (b) 3.8-MoCN; (c) HRTEM image and the inset shows the corresponding SAED pattern of 3.8-MoCN; (d) Cs-corrected HAADF STEM raw image of 3.8-MoCN (e) TEM and (f) HRTEM images of cry-MoCN (inset shows corresponding space lattice of MoO_3); (g) FFT images from the red rectangular area; (h) SAED pattern of cry-MoCN.

heterocycles. Comparatively, the binding energy of three-coordinate $N-C_3$ reveals a significant positive shift for the 3.8-MoCN and CN samples, indicating a noticeable decrease in electron density over the three-coordinate $N-C_3$ (sp^3) center. This finding suggests that the $N-C_3$ (sp^3) is surrounded by many more two-coordinate $C-N=C$ (sp^2) bonds that can capture electrons from $N-C_3$ (sp^3), reflecting the highly condensed aromatic CN heterocycles. The integrated peak area of C 1s and N 1s are provided in Table 1 to obtain further information regarding chemical states and surface chemistry. Remarkably, the $N-C=N$ to $C-C$ and $C-N=C$ (sp^2) to $N-C_3$ (sp^3) area ratios increase for CN compared to BCN, showing the improvement in the polycondensation process resulting in more heptazine units.

Fig. 1e shows the high-resolution XPS spectrum of the Mo 3d core level for the as-prepared MoO_3 and 3.8-MoCN. The pure MoO_3 showed two asymmetric peaks, which were deconvoluted to four peaks at 231.6, 232.7, 234.7, and 235.8 eV. The main peaks at 232.7 and 235.8 eV were assigned to the Mo $3d_{3/2}$ and $3d_{5/2}$ components, respectively, which is indicative of a predominant Mo^{6+} oxidation state [22]. Two additional small peaks at 231.6 and 234.7 eV are attributed to the Mo^{5+} oxidation state, which is consistent with reports in the literature [23]. This presence of Mo^{5+} originated from oxygen vacancy in the as-prepared MoO_3, suggesting that the current synthesis condition with a closed lid can prevent oxygen penetration into the crystallization reaction. Two asymmetric peaks were also observed for 3.8-MoCN, in which four peaks at 231.2, 232.3, 234.4, and 235.5 eV were well fitted, as shown in Fig. 1e. The peaks at 232.3 and 235.5 eV were associated with the Mo^{6+} oxidation state while those at 231.2 and 234.4 eV were assigned to the Mo^{5+} oxidation state. Comparatively, 3.8-MoCN showed much more oxygen vacancies than the as-prepared MoO_3, originating from a strong reduction ability induced by N-coordinating cavities of heptazine units. More importantly, a clear shift of the Mo 3d core level towards lower binding energies is seen for 3.8-MoCN, indicating more electron density on the Mo 3d core level. Therefore, N-coordinating cavities can act as electron donors and stabilize the non-crystalline MoO_3 species within the CN surface. A similar result was observed in the contact of MoO_3 deposited on graphene, where Mo^{5+} increased because of the strong reduction process induced by graphene [24]. In addition, the electrons in the heptazine units tend to transfer to the O-Mo bond, which promotes

the separation of photogenerated charge carriers. Hence, non-crystalline MoO_3 anchored into N-coordinating cavities can improve the homo-dispersion feature of the photocatalyst and provide more surface contact sites without aggregation. The O 1s spectra of 3.8-MoCN were decon-voluted at 530.6 and 532.3 eV, as shown in Fig. S1, corresponding to the lattice oxygen and the surface non-lattice oxygen, respectively [25]. Based on the atomic percentage of O 1s and Mo 3d core level from Table 1, $MoO_{2.4}$ species can be embedded within the CN structure. The molybdenum oxide in this study was MoO_3.

TGA in air was used to investigate the precise concentration of mo-lybdenum oxide in the 3.8-MoCN composite. As shown in Figs. 1f, 3.8-MoCN and as-prepared MoO_3 show a prominent weight loss stage at 430 and 525 °C, respectively. Hence, 3.8-MoCN was decomposed at lower temperatures because of molybdenum oxide. Of particular note is that the organic part of the 3.8-MoCN composite was burned completely (weight loss) up to 560 °C, corresponding to the loss of the CN part. Interestingly, a gentle weight increase was noted from 560° to 680°C. This phenomenon was attributed to the re-filling of oxygen vacancies in molybdenum oxide with oxygen at high temperatures in air [26]. This observation is in line with the XPS results. Therefore, the remaining weight at 560 °C was 2.8 wt%, corresponding to $MoO_{2.4}$ species, whereas the remaining weight at 680 °C was 3.8 wt%, presenting the MoO_3 species. This result indicates that the oxygen vacancy concentration was 1.0 wt%.

Fig. 2 presents SEM images of BCN, CN, and 3.8-MoCN samples. BCN shows an irregularly bulk structure with massive aggregates, while smooth lamellas can be seen in CN and 3.8-MoCN (Fig. 2b and c, respectively), indicating the nanosheet domain. This phenomenon can increase the surface area of the photocatalyst and decrease the diffusion length for charge carriers in the nanosheet structure [27]. Moreover, elemental mapping revealed a uniform distribution of C, N, O, and Mo in the 3.8-MoCN (Fig. 2d and e).

HRTEM and selected area diffraction were analyzed to determine the formation of non-crystalline molybdenum oxide anchored into N-coor-dinating sites. Fig. 3a and b present the nanosheet morphologies of thin CN and 3.8-MoCN; there was no significant difference between them. A high-magnification image (Fig. 3c) showed no lattice spacing related to MoO_3 nanoparticles, confirming the non-crystalline features of MoO_3. In
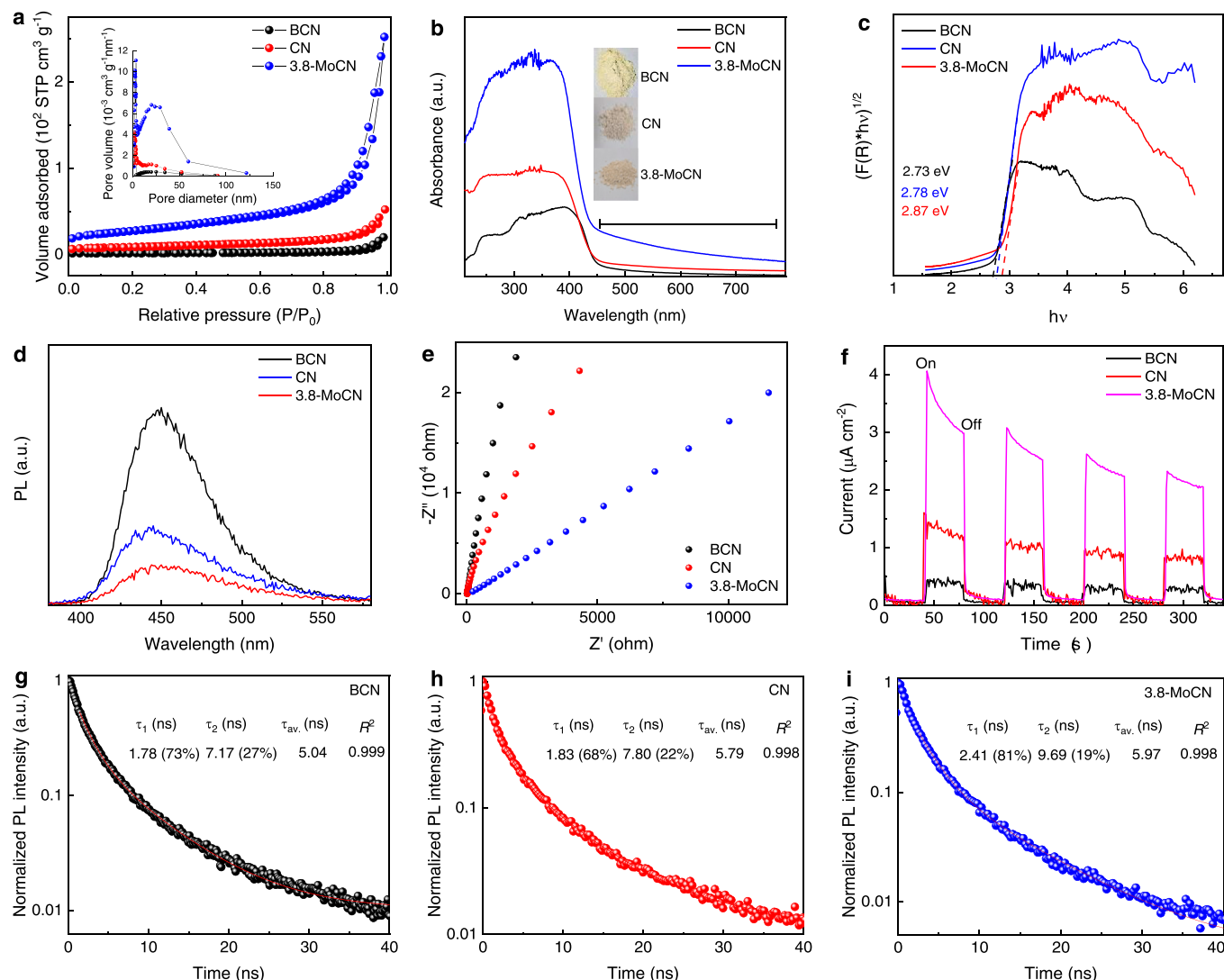
Fig. 4. (a) N_2 adsorption−desorption isotherms, (b) UV–vis/DRS spectra, (c) Tauc plots, (d) PL spectra, (e) EIS Nyquist plots, (f) Photoelectrochemical responses, and (g-i) TRPL spectra of BCN, CN, and 3.8-MoCN (inset shows corresponding fitting data).

addition, no bright spots appear in the selected area diffraction (SAED) pattern, arising from non-crystalline MoO_3 species (inset in Fig. 3c). Further analysis of the 3.8-MoCN was conducted by high-angle annular dark-field scanning transmission electron microscopy (HAADF STEM), as shown in Fig. 3d. Impressively, the raw STEM image revealed an excellent molecular-level distribution with the high quantity of isolated molybdenum oxide anchored on carbon nitride. The bright spots reflected the Mo cluster with heavy molecular mass, which induced a local built-in electric field in CN [28]. This result is consistent with the XRD pattern and XPS investigations discussed above. A heterojunction between CN and high crystalline MoO_3, cry-MoCN, was obtained by prolonging the polycondensation reaction time, as explained in the experimental part. Fig. 3e shows a TEM image of the cry-MoCN, in which MoO_3 nanoparticles were deposited on the CN nanosheets. The magnified TEM image of the cry-MoCN hybrid illustrates the intimate contact between the MoO_3 nanoparticle and CN (Fig. 3f). The HRTEM image of the cry-MoCN along with the FFT filter from the red rectangular area shows distinct lattice fringes with an interplanar distance of 0.37 nm (Fig. 3g), corresponding to the (002) crystal plane of MoO_3 [29], which can be evidenced by the SAED (Fig. 3h) and XRD patterns (Fig. S2).

3.2. Textural and optical properties

The nitrogen adsorption measurements illustrate that the surface area increases in the order of 3.8-MoCN (95.3 m^2 g^{-1}) > CN (30.6 m^2 g^{-1}) > BCN (5.8 m^2 g^{-1}), and pore volume also increases in the similar trend of 3.8-MoCN (0.38 cm^3 g^{-1}) > CN (0.076 cm^3 g^{-1}) > BCN (0.030 cm^3 g^{-1}). Hence, each modification step enhances the textural properties. As displayed in Fig. 4a, all samples unveil the mesoporous texture with the hysteresis loop of the H3-type [30], meaning slit-shaped pores originating from an assembly of rigidly connected particles, which are loosely coherent with no adsorption limitation at high relative pressures (0.9 < P/P_0 < 1). For 3.8-MoCN, the pore size distribution became more homogenous from a set of pores size centered at 20 nm, suggesting that the MoO_3 species can provide more uniform channels. Such an architecture with thin nanosheets increases the surface area and mass transfer from the bulk to the photocatalyst surface and improves multiple scattering effects. Isolated MoO_3 species anchored on the CN surface can, in turn, enhance the catalytic contact sites and, consequently, the photocatalytic activity.

The light-harvesting ability of synthesized samples was examined by UV–vis/DRS spectroscopy. As predicted, BCN has just an absorption edge around 450 nm with weak intensity, reflecting the lack of visible light activity (Fig. 4b). Compared to BCN, the absorption intensity of CN
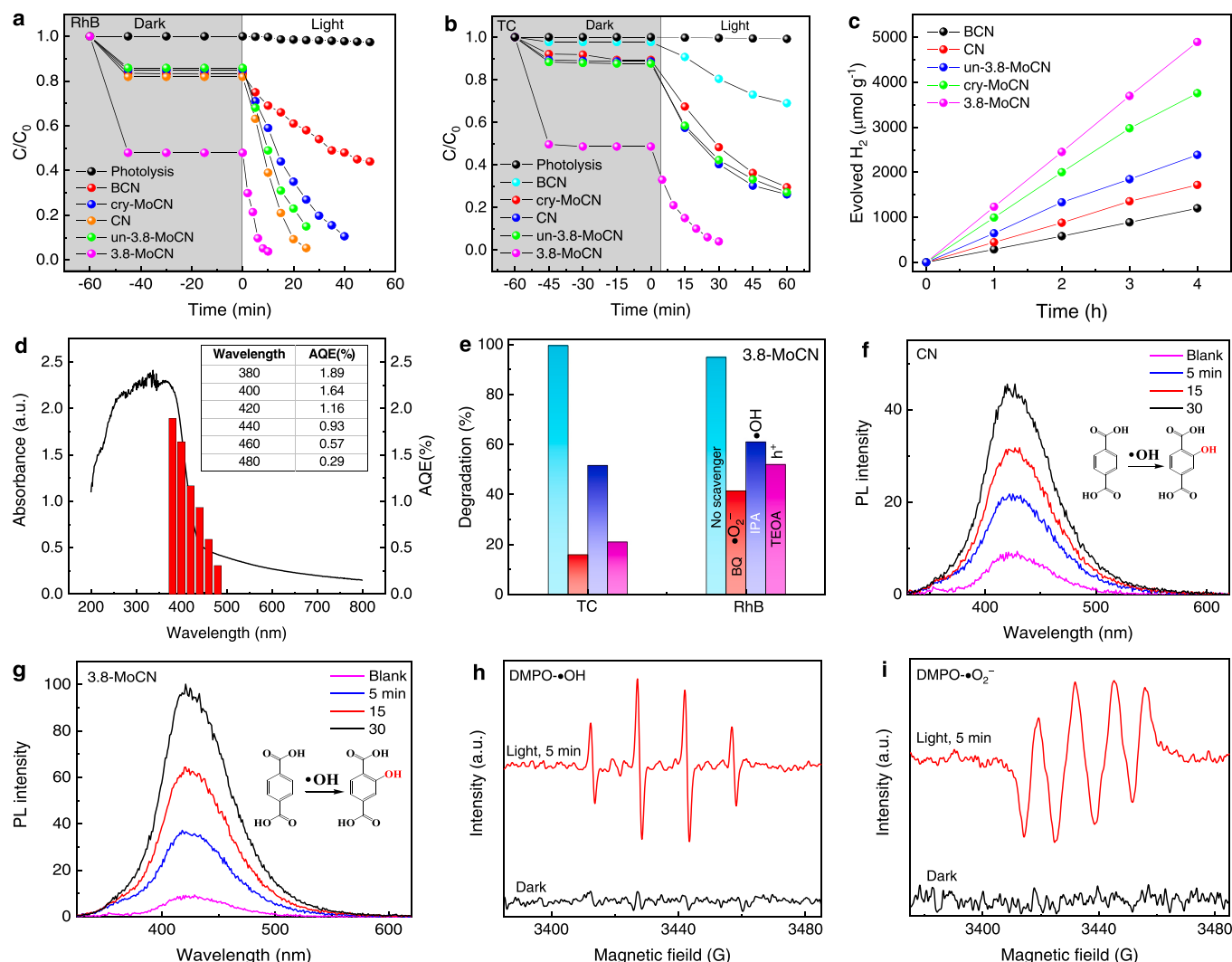
Fig. 5. Photocatalytic degradation of (a) RhB and (b) TC using BCN, CN, cry-MoCN, and 3.8-MoCN; (c) Comparison of the photocatalytic H_2 production of BCN, CN, cry-MoCN, and 3.8-MoCN using 20 v% triethanolamine (TEOA) aqueous solution as a sacrificial reagent and 1 wt% Pt under visible-light irradiation ($\lambda \geq 400$ nm, 300 W Xe lamp); (d) Absorption and action spectrum (apparent quantum efficiency) of 3.8-MoCN for the degradation of RhB; (e) Scavenging results for TC and RhB over 3.8-MoCN; (f and g) the PL spectra of the produced 2-hydroxyterephthalic acid over CN and 3.8-MoCN; (h and i) ESR spectra of 3.8-MoCN for identifying DMPO-•OH and DMPO-•O_2^- under dark and visible light illumination.

increased gradually and extended the absorption range of visible light to 800 nm. This improvement originated from the highly condensed structure of heptazine units acting as visible light antennae. Remarkably, 3.8-MoCN exhibited a very strong absorption peak along with a prominent absorption tail in the range of visible and NIR light. This tail can demonstrate isolated MoO_3 species embedded in the six-fold cavities of CN, which might show a quantum confinement effect, such as metal particles. A similar result was observed for tungsten oxide with abundant oxygen vacancies elsewhere [31]. MoO_3 with intrinsic oxygen vacancies can also harvest visible light irradiation, leading to enhancement compared to CN. Therefore, the production and accessibility of photoexcited charges eventually increase because of the highly conjugated heptazine structure and well-distributed MoO_3 surface active sites, respectively. This result is in line with the lowest crystallinity of MoO_3, the highest dispersion, and lower aggregation. The color of the 3.8-MoCN sample changed from yellow to light gray, which is consistent with the change in absorbance. The bandgap of each photocatalyst was calculated from a Kubelka–Munk plot (Fig. 4c). The bandgaps of BCN, CN, and 3.8-MoCN were 2.73 eV, 2.78 eV, and 2.87 eV, respectively. The bandgap increased by changing the morphology. The highest one for 3.8-MoCN is due to a decrease in nanosheet thickness and its quantum

confinement effect. Moreover, the direct band gap of MoO_3 was estimated to be 3.11 eV (Fig. S3).

3.3. Charge separation and electronic band structure

The steady-state PL emission intensity, arising from the intrinsic HOMO-LUMO transition, provides more information on the recombination of charges. Under an excitation light of 365 nm, CN exhibits weaker emission than that of the BCN, suggesting that the charge recombination is suppressed after thermal polycondensation of supramolecular self-assembly (Fig. 4d). CN has a more condensed structure and improved textural properties, as confirmed by the XPS and BET measurements. Moreover, the 3.8-MoCN has the lowest PL intensity, suggesting that the combination of photogenerated charges is inhibited significantly after embedding non-crystalline MoO_3 into the conjugated structure of CN. Electrochemical methods, such as EIS and the transient photocurrent (I-t) response, are effective means to determine the electron transfer rate at the electrode/electrolyte interface. Fig. 4e shows the Nyquist plots of BCN, CN, and 3.8-MoCN. Among them, 3.8-MoCN shows the smallest semi-circle in the Nyquist plot, accrediting more effective charge transfer and less charge resistance at the photocatalyst/

electrolyte interface [32]. Hence, MoO_3 on the CN surface accelerates charge transfer and provides many more channels for improving the charge transitions. This can be confirmed by the transient photocurrent (I-t) response, as shown in Fig. 4**f**. The 3.8-MoCN showed great enhancement in the photocurrent response as soon as the visible light source was turned on compared to other samples. The more than double elevation of the charge mobility in 3.8-MoCN was because the nanosheet morphologies of CN strengthen charge separation and transition from its bulk phase to the surface. Consequently, MoO_3 centers located in the heptazine cavities accelerate the electron transfer kinetics.

The time-resolved transient PL (TRPL) decay technique was applied to gain additional information on the lifetime of the photogenerated charge carrier. TRPL curves can be fitted with a bi-exponential model, as indicated in Eq. 9, where τ_1 is the short lifetime with amplitude A_1 and τ_2 is the long lifetime with amplitude A_2. The average emission lifetime $(\tau_{av.})$ was calculated using Eq. 10.

$$I(t) = A_1 \exp(-t/\tau_1) + A_2 \exp(-t/\tau_2) \tag{9}$$

$$\tau_{av.} = \left(A_1\tau_1{}^2 + A_2\tau_2{}^2\right)/\left(A_1\tau_1 + A_2\tau_2\right) \tag{10}$$

τ_1 and τ_2 resulted from non-radiative relaxation and inter-band recombination of free excitons, respectively [33]. The non-radiative relaxation has an inverse trend with the fluorescence quantum yield, meaning the more non-radiative relaxation can favor higher photocatalytic performance [8]. In addition, non-radiative relaxation is promoted by structure distortion, local defects, and foreign atoms [34]. As listed in the inset of Figs. 4**g-i**, 3.8-MoCN effectively extends the lifetime (5.97 ns) compared to CN (5.79 ns) and BCN (5.04 ns). In addition, the amplitude of non-radiative relaxation (81%) for 3.8-MoCN was more than CN (68%) and BCN (73%), highlighting the effective separation of photogenerated electron–hole pairs. This can result from molybdenum catalytic centers, which increase internal conversion and intersystem crossing, enhancing the non-radiative component.

3.4. Photocatalytic activities

3.4.1. Photocatalytic degradation

The photocatalytic performance of 3.8-MoCN was evaluated primarily by photocatalytic degradation of stable RhB as the reference pollutant and then the antibiotic TC. RhB and TC are persistent under visible light irradiation, meaning the photolysis effect can be ignored, as shown in Fig. 5. Before light irradiation, all samples were placed in the dark to reach the adsorption–desorption equilibrium between contaminant molecules and photocatalyst surface. As shown in Fig. 5**a**, compared to BCN and CN, the 3.8-MoCN sample showed enhanced visible-light activity towards RhB photodegradation within just 10 min. More than 95% degradation occurred over 3.8-MoCN after 10 min light $(\lambda \geq 400$ nm), while 59% and 30% degradation occurred for CN and BCN, respectively. Hence, the apparent rate constant (k_{app}) of RhB over 3.8-MoCN (0.276 min^{-1}) was approximately 21.7 times more than that of BCN (0.0127 min^{-1}) (Fig. S4a). The 3.8-MoCN could also degrade TC within 30 min under visible-light illumination $(\lambda \geq 400$ nm). As shown in Figs. 5**b**, 3.8-MoCN degraded up to 96% of TC within 30 min, whereas 60% and 20% degradation was noted over CN and BCN. Among the three samples, 3.8-MoCN possessed the highest k_{app} for TC degradation under visible light, which is approximately 13.6 times as high as that of BCN (Fig. S4b). It is worth noting that the photocatalytic performance of pure CN is very similar to un-3.8-MoCN, indicating that the annealing step might strength the MoO_3 with CN skeleton. Therefore, 3.8-MoCN shows tremendously enhanced photodegradation than other control samples. Interestingly, the photocatalytic activity of the as-prepared cry-MoCN toward both RhB and TC degradation was much less than that of 3.8-MoCN, meaning that high-dispersed non-crystalline MoO_3 improved the photocatalytic efficiency further. This result can be attributed to the harsh reaction temperature used to grow the regular arrangement of MoO_3 with crystalline properties on the CN material, giving a strong

interface (see HRTEM). Under this condition, the CN component is susceptible to sublimation, losing a significant part of its heptazine units and decreasing its performance. The photocatalytic activity of 3.8-MoCN was compared with the activities of other metal oxide-based heterojunction photocatalysts (Table S1). The apparent quantum efficiency of 3.8-MoCN was also calculated to compare the efficiency under the monochromated illumination. The 3.8-MoCN shows AQE of 1.64% at 400 nm while the AQE for CN, un-3.8-MoCN, cry-MoCN, and BCN are 0.53%, 0.55%, 0.62%, and 0.0% at 400 nm, respectively (Fig. 5**d**). The 3.8-MoCN photocatalyst has full advantage of their principle manipulations, which include highly condensed tri-s-thiazine units with nanosheet features and many isolated non-crystalline MoO_3 species. The stability of 3.8-MoCN was evaluated by recycling tests for RhB degradation under visible light (Fig. S5a). After five cycles, the degradation efficiency exhibited a slight decrease of 11.4%, which was attributed to the mass loss after the mechanical treatment, such as washing, centrifuging, and drying. No significant change was observed in the XRD pattern (Fig. S5b), indicating the preservation of the framework after the repeated experiments.

3.4.2. Photocatalytic H_2 production

All the synthesized photocatalysts were assessed for photocatalytic H_2 production, in which the surface-active sites and quantity are crucial for proton adsorption and electron accumulation. A low amount of 1 wt % Pt was used as a cocatalyst to unveil the surface chemical capability of the samples. The actual amount of Pt loaded on the catalyst was obtained by ICP-OES analysis. The amounts of 1.139, 0.924, 0.929, 1.103, and 1.028 wt% Pt were determined over BCN, CN, un-MoCN, cry-MoCN, and 3.8-MoCN, respectively. In the absence of Pt, the hydrogen evolution is trace and insignificant. As shown in Fig. 5**c**, the hydrogen evolution rate (HER) for BCN was 264 µmol g^{-1}h^{-1}, whereas the HER for CN was 441 µmol g^{-1}h^{-1}. This obvious improvement arises from the enlarged surface area, better electron–hole transfer, and boosted heptazine units. The initial HER rate for 3.8-MoCN was 1265 µmol g^{-1}h^{-1}, which is a factor of 4.7 and 2.8 higher than that of the BCN and CN, respectively. The apparent enhancement of 3.8-MoCN in the HER was attributed to the significant increase in the visible-light threshold from 450 to 800 nm, excellent surface area, and charge transfer rate. This finding shows that isolated non-crystalline molybdenum oxide anchored on carbon nitride provides more active sites for proton adsorption and electron accumulation. Interestingly, the HER performance of 3.8-MoCN with isolated non-crystalline molybdenum oxide was much higher than cry-MoCN with a strong heterojunction interface. As a result, the latter possess fewer surface-active sites per gram of photocatalyst. The HER stability test of the 3.8-MoCN sample over three repeated operations confirms the photocatalytic H_2 production nature (Fig. S5c).

3.5. Study of the active species, DFT simulation, and photocatalytic mechanism

Trapping experiments were conducted to explore the role of active species in the photocatalytic degradation processes. BQ, IPA, and TEOA were selected as capturing molecules for $\bullet O_2^-$, $\bullet OH$, and h^+ [35] As shown in Fig. 5**e**, the RhB degradation activity on 3.8-MoCN decreases significantly after adding BQ, IPA, and TEOA solutions, suggesting that all three species are the dominant reactive species that contributed to the photocatalytic activity. Similarly, TC degradation was also suppressed in the presence of BQ, IPA, and TEOA scavengers, uncovering that the $\bullet O_2^-$, $\bullet OH$, and h^+ play a pivotal role in the degradation of TC. A series of experiments were performed using fluorescence spectroscopy to explain the role of the $\bullet OH$ concentration. $\bullet OH$ radicals can react with terephthalic acid (TA), a probing molecule, to produce 2-hydroxy-terephthalic acid with high fluorescence properties. Hence, the fluorescence intensity is in proportion to the $\bullet OH$ concentration. As shown in Fig. 5**f** and **g**, an increasing trend of fluorescence intensities can be observed for both suspensions of CN and 3.8-MoCN, suggesting the
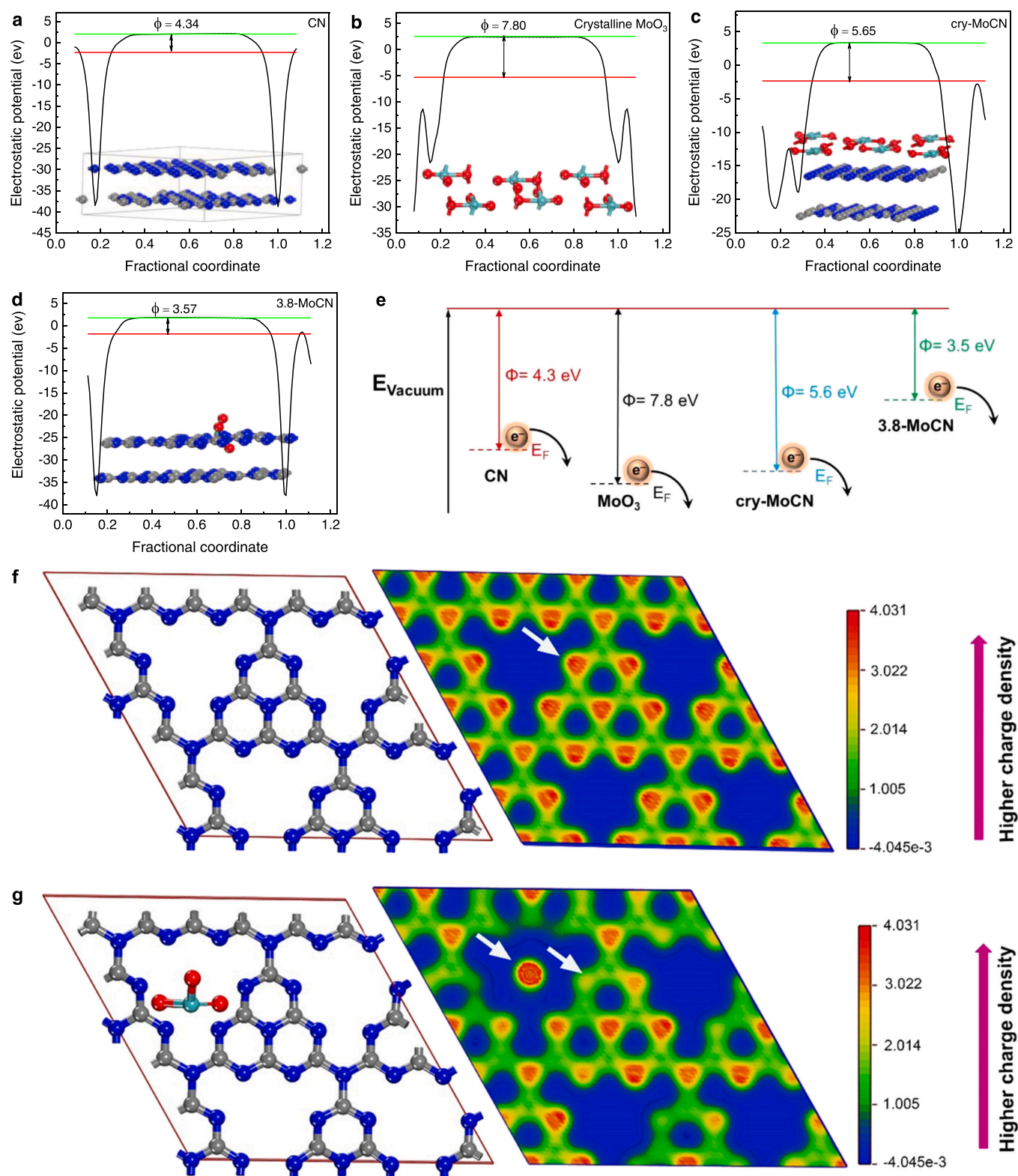
Fig. 6. Simulated work functions (Φ) of (a) pure CN, (b) crystalline MoO₃, (c) cry-MoCN heterojunction, and (d) 3.8-MoCN photocatalyst; (e) the estimation of Fermi levels. Charge difference distribution over (f) pure CN and (g) 3.8-MoCN photocatalysts.

gradually enhanced •OH concentrations in the photocatalytic systems by prolonging the time. In particular, strong intensities can be seen in the case of 3.8-MoCN, revealing more efficient photogenerated electron–hole pairs (Fig. 5g).

Moreover, EPR analysis was recorded to measure the presence of

•O₂⁻ and •OH caused by 3.8-MoCN under dark and light conditions (λ ≥ 400 nm). As shown in Fig. 5h and i, neither DMPO-•OH nor DMPO-•O₂⁻ was detected in the dark. Conversely, a strong quartet of 1:2:2:1 relative intensity ratio was detected after 5 min irradiation time, which was characteristic of the DMPO-•OH adduct (Fig. 5h). Similarly, Fig. 5i
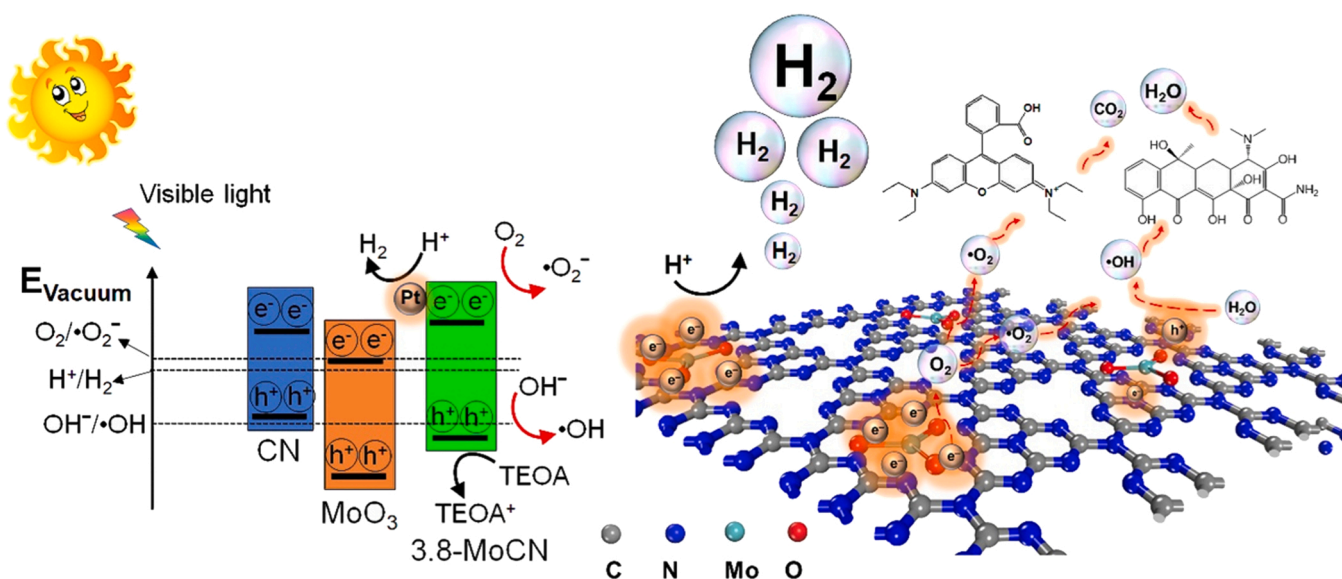
Fig. 7. (left) Schematic energy band diagram of MoO_3 and CN; (right) Schematic illustration of the photodegradation mechanism of TC/RhB and photocatalytic H_2 production over the 3.8-MoCN photocatalyst.

indicates a robust EPR signal with a 1:1:1:1 intensity ratio, indicating the formation of DMPO-$\bullet O_2^-$. As a result, the 3.8-MoCN photocatalyst can generate large amounts of $\bullet O_2^-$ and $\bullet OH$ radicals in a very short time under visible-light illumination.

The energy band structure of BCN, CN, and 3.8-MoCN need to be estimated to reveal the photocatalytic mechanism. This study performed the Mott–Schottky measurements to calculate the flat band potentials (V_{fb}) of the prepared samples. This analysis is based on the capacitance versus the applied potential according to Eq. (11).

$$\frac{1}{C^2} = \frac{2}{\varepsilon\varepsilon_0 A^2 e N_D}\left(V - V_{fb} - \frac{K_B T}{e}\right) \tag{11}$$

where C is the space charge capacity; ε is the dielectric constant of the semiconductor; ε_0 is the vacuum permittivity; N is the donor concentration per unit volume; A is the active surface area; V is the applied potential at the electrode; k is the Boltzmann constant. The x-intercept obtained from a plot of C^{-2} versus the applied potential (V) was interpreted as V_{fb} [36]. From Fig. S6, all samples exhibited positive slopes with n-type properties, indicating that electrons are the majority carriers. From the electrochemical point of view, the flat band potentials of BCN, CN, and 3.8-MoCN were determined to be –0.79, –0.89, and −1.20 V (vs. Ag/AgCl), respectively. Hence, the flat band potentials of BCN, CN, and 3.8-MoCN are –0.59, –0.67, and −1.0 V vs. NHE, respectively. 3.8-MoCN showed an elevated negative flat band position. Because their V_{fb} position in n-type semiconductors is very close to their CB, their VB position was estimated from the band gap derived from the Tauc plot. Therefore, the VB of the CN with new morphology can be determined to be 1.87 V (vs. NHE). The VB of MoO_3 was calculated using the electronegativity concept in Eqs. (12) and (13) [37], where E_{CB} and E_{VB} indicate the energy levels of CB and VB, respectively; E_g is the band gap of MoO_3 (3.11 eV); E^e (4.5 eV) is the free electron energy on the hydrogen scale; χ denotes the electronegativity of the semiconductor, which is 6.40 eV for MoO_3 [25]. Hence, the VB and CB values for MoO_3 were 3.45 and 0.34 eV.

$$E_{VB} = \chi - E^e + 0.5E_g \tag{12}$$

$$E_{CB} = E_{VB} - E_g \tag{13}$$

Compared with BCN and CN, the E_{fb} of 3.8-MoCN is shifted negatively, suggesting a higher Fermi level of 3.8-MoCN. A more negative Fermi level can provide more driving force for accelerating electron

transport. As a result, MoO_3 species with high distribution provided a new channel for trapping and transferring electrons, which is crucial for photocatalytic systems.

To understand the work function (Φ) and corresponding Fermi level positions at a complexity environment of non-crystalline MoO_3, density functional theory (DFT) was applied, as shown in Fig. 6a-d. The Fermi levels of crystalline MoO_3, non-crystalline MoO_3 anchored to N-coordinating cavities of CN (3.8-MoCN), pristine CN, and also a heterojunction of the crystalline MoO_3 nanoparticles deposited on the CN sheets (cry-MoCN) were simulated. The work functions for pristine MoO_3, pristine CN, 3.8-MoCN, and cry-MoCN were 7.80, 4.34, 3.57, and 5.65 eV, respectively. Interestingly, the 3.8-MoCN sample exhibited an elevated work function (lower Fermi level) compared to cry-MoCN, indicating the increase of electron mobility and charge transition on 3.8-MoCN (Fig. 6e). This computational result and experimental evidence strongly suggest that the design of new heterogeneous isolated metal oxide catalysts can surpass the activity of conventional heterojunction catalysts.

To get insight into the charge carrier's separation and movement, charge distribution properties were further explored by the DFT calculations. Fig. 6f and g reveals the charge density distribution around the atoms in 3.8-MoCN and also pure CN for comparison. The positive and negative values indicate electron accumulation and depletion, corresponding to the red and blue areas, respectively. Blue, gray, red, and turquoise spheres denote N, C, O, and Mo atoms. Fig. 6f illustrates that the electrons are accumulated largely in the N atoms (see white arrow) for the pure CN. It also shows symmetric charge distributions throughout the pure CN, resulting in more chance of charge recombination. On the other hand, for the 3.8-MoCN, Fig. 6g unveils that the electrons are accumulated largely in the MoO_3, while they are depleted in the CN nanosheet (see white arrow). This can be a result of a built-in electric field that is produced around the interface. It appears that the MoO_3 acts as an electron trap to accelerate charge separation providing more delocalized electrons in 3.8-MoCN rather than in pure CN. Meaning the electric field of MoO_3 changes the distribution of electrons which promotes the separation of electron-hole pairs.

Fig. 7 shows the electronic band structures of 3.8-MoCN based on the above analysis. The photocatalytic mechanism of the 3.8-MoCN hybrid system is also proposed schematically in Fig. 7. Owing to the intrinsic feature of CN and MoO_3 as one of the strongest reduction and oxidation semiconductors, respectively, their band edge potentials are staggered,
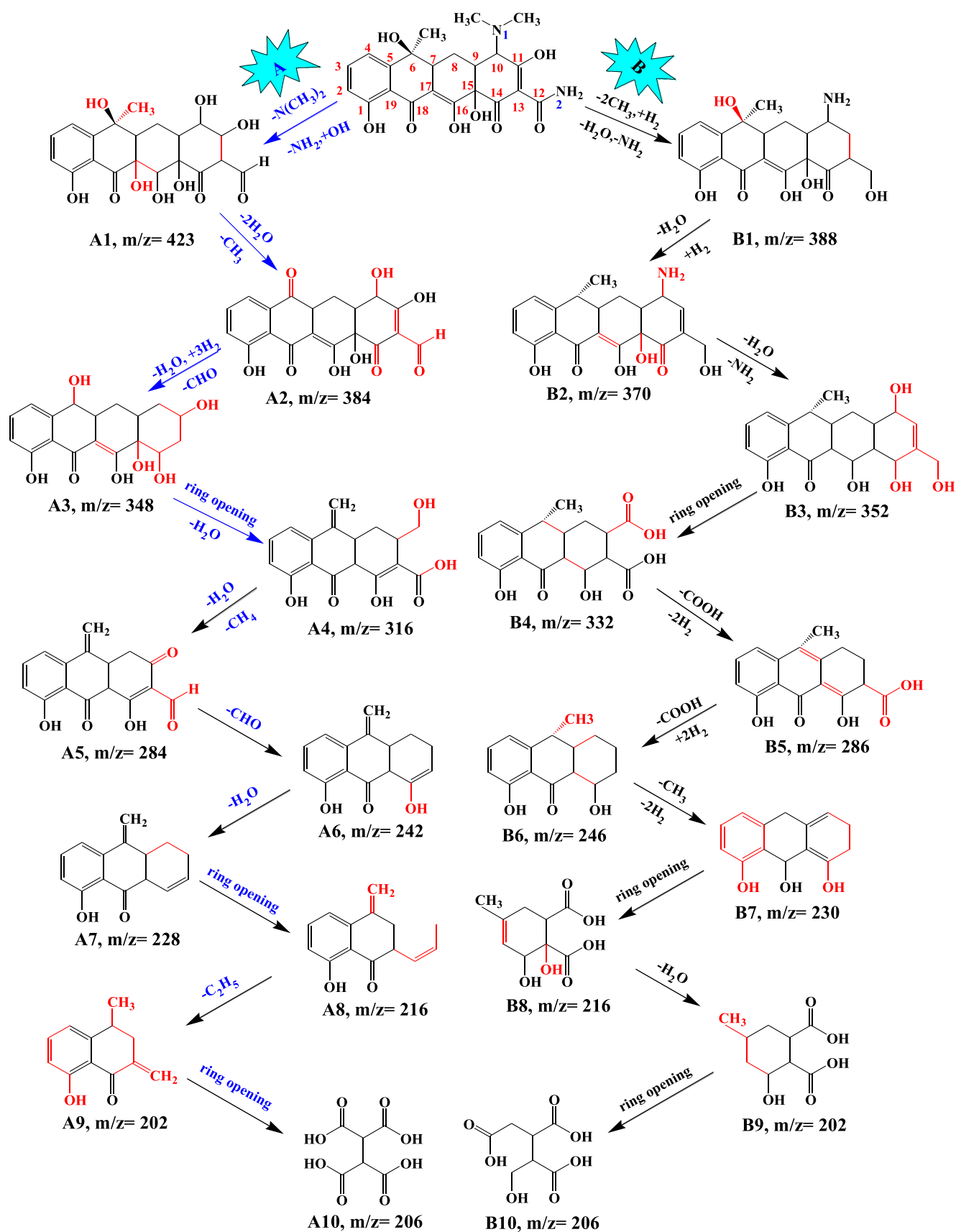
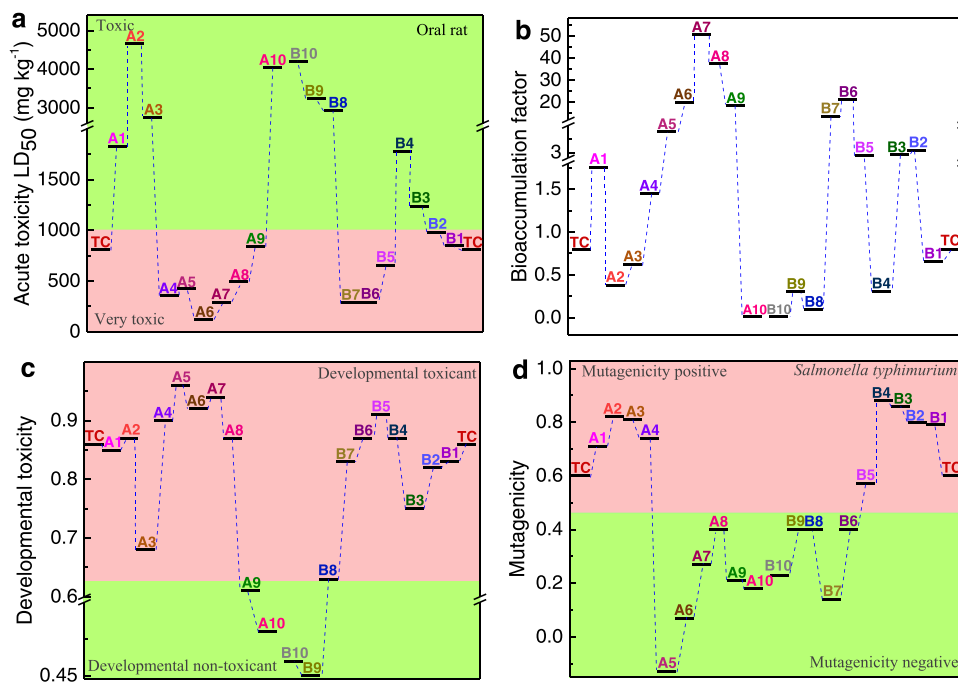**Scheme 2.** Possible pathways of TC photodegradation over the 3.8-MoCN photocatalyst.

Fig. 8. Toxicity assessment results of TC intermediates produced under photocatalytic degradation over 3.8-MoCN photocatalyst (a) acute toxicity LD_{50}, (b) Bioaccumulation factor, (c) developmental toxicity, and (d) mutagenicity.

and they can make an effective migration pathway for charge carriers. When the 3.8-MoCN is irradiated with visible light, both CN nanosheets and MoO_3 with high oxygen vacancies are excited to generate electron–hole pairs. PL spectroscopy and EPR results showed that the highest concentration of $\bullet OH$ and $\bullet O_2^-$ could be generated over 3.8-MoCN. Thus, the spatial charge separation leads to electrons and holes with the strongest reduction and oxidation abilities on the CB and VB of 3.8-MoCN, respectively. Thus, the holes might overcome the barrier for the $OH^-/\bullet OH$ half-reaction (1.99 eV) [38]. On the other hand, the accumulated electrons on the CB of 3.8-MoCN can immediately react with dissolved oxygen molecules to generate $\bullet O_2^-$ ($O_2/\bullet O_2^-$, ‑‑0.33 eV) [28]. Thus, $\bullet OH$ and $\bullet O_2^-$ can be formed effectively over 3.8-MoCN to eliminate aqueous TC and RhB pollutants. In addition, Mo–O can store multiple electrons, which is very helpful for charge separation and H_2 evolution from H^+ [39]. On the basis of the computational and experimental results, 3.8-MoCN can absorb visible light to generate electrons and holes throughout the photocatalyst network. Moreover, the presence of isolated molybdenum oxide anchored on carbon nitride can tune optical properties and provide new catalytic sites while accelerating the rapid transfer of electron-hole pairs. The electrons with a long life-time attend in the reduction reaction of protons to evolve hydrogen (HER). Indeed, the hydrogen atoms are derived partly from water splitting and partly from the dehydrogenation of the TEOA as a hole scavenger. TEOA has 15 hydrogen atoms and reacts with holes on the VB to produce the oxidized TEOA (TEOA$^\bullet$). The hole in the VB is also filled by the electron from the scavenger, further increasing the life-time of the electron in the CB, boosting hydrogen evolution.

3.6. Identification of intermediates and degradation pathways of TC

The properties of the TC degradation products were analyzed by LC-MS/MS after 5, 15, and 30 min, and degradation mechanisms were proposed. Significant loss of the TC peak ($m/z = 445$) after 5 min, and the new products showed high-performance of 3.8-MoCN to degrade TC (Fig. S7). According to the literature, Scheme 2 introduces two proposed degradation mechanisms. Based on pathway A, the intermediate A1 ($m/z = 423$) appeared by a reaction on both nitrogen sites (N1 and N2) of the parent TC and removing $-N(CH_3)_2$ and $-NH_2$ groups.

Subsequently, A2 ($m/z = 384$) is produced by dehydroxylation and demethylation. The aldehyde functional group was removed, followed by dehydroxylation and hydrogenation reactions to form A3 with $m/z = 348$. The intermediate of A4 ($m/z = 316$) was generated through a ring opening and dehydration reaction on C6. In the next parts, two rings containing C1–C7 and C17–C19 were almost unchanged during the four steps while dehydration, dealkylation, removing $-CHO$ group, and ring-opening process formed A5 ($m/z = 284$), A6 ($m/z = 242$), A7 ($m/z = 228$), and A8 ($m/z = 216$) products, respectively. Finally, dealkylation and ring-opening reactions promoted the generation of A9 ($m/z = 228$) and A10 ($m/z = 216$). In pathway B, deamination at C12 and demethylation of the N1 site of TC lead to the production of B1($m/z = 388$). Dehydroxylation and hydrogenation reactions converted B1 to B2 ($m/z = 370$). Product B3 ($m/z = 352$) was formed during dehydration, hydrogenation reaction, and changes of $-NH_2$ to $-OH$ groups. Ring-opening, loss of $-COOH$, hydrogenation, dehydrogenation, and demethylation reactions generated B4 ($m/z = 332$), B5 ($m/z = 286$), B6 ($m/z = 246$), B7 ($m/z = 230$), and B8 ($m/z = 216$) intermediates. The removal of a water molecule within hydrogenation produced B9 ($m/z = 202$), while B10 ($m/z = 206$) was obtained via a ring-opening process.

3.7. Toxicity evaluation

A variety of intermediates were produced through the photodegradation process is generated. Therefore, their toxicity during the reaction for the complete removal of effluent pollution was examined. In this regard, the Toxicity Estimation Software Tool (T.E.S.T.) was used to assess the acute toxicity, bioaccumulation factors, developmental toxicity, and mutagenicity toxicity parameters of intermediates using the quantitative structure-activity relationship (QSAR) technique. Fig. 8 shows the toxicity assessment parameters for TC and 20 estimated intermediates. The acute toxicity for TC and intermediates showed that approximately 40% of intermediates had an LD_{50} (rat, oral) of more than 2000 mg kg^{-1} that had been assigned to category 5 of the Globally Harmonized System (Fig. 8a) [40]. In particular, 70% of the degradation products had less toxicity within pathway B than TC. Although most of the intermediates in pathways A and B have bioaccumulation factors

(BCF) and the values of developmental toxicity more than TC, these parameters for the final products are lower than TC (see Fig. 8**b, c**). As illustrated in Fig. 8**d**, in pathway A except for A1-A4, all products were mutagenicity negative, while in pathway B, except for B1 to B5, the other final products were mutagenicity negative. These results show that the photodegradation process reduces the toxicity of TC in just 30 min. However, it is not enough to achieve complete non-toxic effluent, and expanding the reaction time may be desirable.

4. Conclusions

This study showed that non-crystalline molybdenum oxide could be confined to N-coordinating cavities of highly condensed carbon nitride (3.8-MoCN). This enables the design of isolated MoO_3 species anchored to six-fold pores of heptazine units, preventing aggregation, as confirmed by molecular dynamics simulations. Therefore, more catalytic contact sites and distribution are obtained on the CN surface, which is crucial for accelerating charge transfer and performance. The photocatalyst comprises isolated MoO_3 species, similar to single-site atom catalysts. In addition, it demonstrates well-matched band structures between the MoO_3 species and CN semiconductors, as seen in heterojunction-based catalysts, promoting interfacial carrier transfer. The highest photocatalytic activity was obtained toward the degradation of TC and RhB (over 96% within 30, and 10 min, respectively). 3.8-MoCN exhibited a HER rate of 1265 $\mu mol\ g^{-1}h^{-1}$, which is a factor of 4.7 and 2.8 higher than that of the BCN and CN, respectively. The degradation pathway of TC and its intermediates were investigated by LC–MS/MS. Moreover, the toxicity assessment of the TC intermediates showed that TC is degraded to fragments with a higher lethal dose (LD_{50}) and less toxicity. This research can provide a new opportunity for heterogeneous photocatalysis conjugating with non-crystalline metal oxides to improve the performance to a great level.

CRediT authorship contribution statement

Milad Jourshabani: Conceptualization, Methodology, Data curation, Writing – original draft. **Mahdieh Razi Asrami:** Software, Writing – review & editing. **Byeong‐Kyu Lee:** Supervision, Writing – review & editing.

Declaration of Competing Interest

The authors declare that they have no known competing financial interests or personal relationships that could have appeared to influence the work reported in this paper.

Data availability

Data will be made available on request.

Appendix A. Supporting information

Supplementary data associated with this article can be found in the online version at doi:10.1016/j.apcatb.2023.122907.

References

[1] W.-J. Ong, L.-L. Tan, Y.H. Ng, S.-T. Yong, S.-P. Chai, Graphitic carbon nitride (g-C_3N_4)-based photocatalysts for artificial photosynthesis and environmental remediation: are we a step closer to achieving sustainability, Chem. Rev. 116 (2016) 7159–7329.

[2] M. Jourshabani, B.-K. Lee, Z. Shariatinia, From traditional strategies to Z-scheme configuration in graphitic carbon nitride photocatalysts: recent progress and future challenges, Appl. Catal. B 276 (2020), 119157.

[3] Y. Cui, J. Zhang, G. Zhang, J. Huang, P. Liu, M. Antonietti, X. Wang, Synthesis of bulk and nanoporous carbon nitride polymers from ammonium thiocyanate for photocatalytic hydrogen evolution, J. Mater. Chem. 21 (2011) 13032–13039.

[4] X. Zhang, X. Ran Zhang, P. Yang, H.-S. Chen, S. Ping, Jiang, Black magnetic Cu-g-C_3N_4 nanosheets towards efficient photocatalytic H_2 generation and CO_2/benzene conversion, Chem. Eng. J. 450 (2022), 138030.

[5] J. Barrio, M. Shalom, Rational design of carbon nitride materials by supramolecular preorganization of monomers, ChemCatChem 10 (2018) 5573–5586.

[6] X. Chen, Y.-S. Jun, K. Takanabe, K. Maeda, K. Domen, X. Fu, M. Antonietti, X. Wang, Ordered mesoporous SBA-15 type graphitic carbon nitride: a semiconductor host structure for photocatalytic hydrogen evolution with visible light, Chem. Mater. 21 (2009) 4093–4095.

[7] Y.-S. Jun, E.Z. Lee, X. Wang, W.H. Hong, G.D. Stucky, A. Thomas, From melamine-cyanuric acid supramolecular aggregates to carbon nitride hollow spheres, Adv. Funct. Mater. 23 (2013) 3661–3667.

[8] M. Shalom, S. Inal, C. Fettkenhauer, D. Neher, M. Antonietti, Improving carbon nitride photocatalysis by supramolecular preorganization of monomers, J. Am. Chem. Soc. 135 (2013) 7118–7121.

[9] Z. Zhou, D. Chen, N. Li, Q. Xu, H. Li, J. He, J. Lu, Three-Dimensional g-C_3N_4/NH_2-UiO-66 graphitic aerogel hybrids with recyclable property for enhanced photocatalytic elimination of nitric oxide, Chem. Eng. J. 418 (2021), 129117.

[10] P. Zhou, J. Yu, M. Jaroniec, All-solid-state Z-scheme photocatalytic systems, Adv. Mater. 26 (2014) 4920–4935.

[11] D. Liu, J. Yao, S. Chen, J. Zhang, R. Li, T. Peng, Construction of rGO-coupled C_3N_4/C_3N_5 2D/2D Z-scheme heterojunction to accelerate charge separation for efficient visible light H_2 evolution, Appl. Catal. B 318 (2022), 121822.

[12] C. Hu, H. Dai, C. Tan, Q. Pan, F. Hu, X. Peng, Photo-Fenton degradation of tetracycline over Z-scheme Fe-g-C_3N_4/Bi_2WO_6 heterojunctions: mechanism insight, degradation pathways and DFT calculation, Appl. Catal. B 310 (2022), 121326.

[13] L. Liu, J. Huang, H. Yu, J. Wan, L. Liu, K. Yi, W. Zhang, C. Zhang, Construction of MoO_3 nanopaticles /g-C_3N_4 nanosheets 0D/2D heterojuntion photocatalysts for enhanced photocatalytic degradation of antibiotic pollutant, Chemosphere 282 (2021), 131049.

[14] G. Wang, T. Zhang, W. Yu, R. Si, Y. Liu, Z. Zhao, Modulating location of single copper atoms in polymeric carbon nitride for enhanced photoredox catalysis, ACS Catal. 10 (2020) 5715–5722.

[15] C. Zhang, D. Qin, Y. Zhou, F. Qin, H. Wang, W. Wang, Y. Yang, G. Zeng, Dual optimization approach to Mo single atom dispersed g-C_3N_4 photocatalyst: Morphology and defect evolution, Appl. Catal. B 303 (2022), 120904.

[16] D. Liu , S. Zhang , J. Wang , T. Peng , R. Li , Direct Z-Scheme 2D/2D Photocatalyst Based on Ultrathin g-C3N4 and WO3 Nanosheets for Efficient Visible-Light-Driven H2 Generation, ACS Appl. Mater. Interfaces 11 (2019) 27913–27923.

[17] Y. Deng, Z. Zhou, H. Zeng, R. Tang, L. Li, J. Wang, C. Feng, D. Gong, L. Tang, Y. Huang, Phosphorus and kalium co-doped g-C_3N_4 with multiple-locus synergies to degrade atrazine: insights into the depth analysis of the generation and role of singlet oxygen, Appl. Catal. B 320 (2023), 121942.

[18] X. She, H. Xu, Y. Xu, J. Yan, J. Xia, L. Xu, Y. Song, Y. Jiang, Q. Zhang, H. Li, Exfoliated graphene-like carbon nitride in organic solvents: enhanced photocatalytic activity and highly selective and sensitive sensor for the detection of trace amounts of Cu2+, J. Mater. Chem. A 2 (2014) 2563–2570.

[19] J. Jiang, X. Wang, C. Yue, S. Liu, Y. Lin, T. Xie, S. Dong, Efficient photoactivation of peroxymonosulfate by Z-scheme nitrogen-defect-rich NiCo2O4/g-C3N4 for rapid emerging pollutants degradation, J. Hazard. Mater. 414 (2021), 125528.

[20] M. Jourshabani, M.R. Asrami, B.-K. Lee, An efficient and unique route for the fabrication of highly condensed oxygen-doped carbon nitride for the photodegradation of synchronous pollutants and H_2O_2 production under ambient conditions, Appl. Catal. B 302 (2022), 120839.

[21] V.D. Dang, T. Annadurai, A.P. Khedulkar, J.-Y. Lin, J. Adorna, W.-J. Yu, B. Pandit, T.V. Huynh, R.-A. Doong, S-scheme N-doped carbon dots anchored g-C_3N_4/Fe_2O_3 shell/core composite for photoelectrocatalytic trimethoprim degradation and water splitting, Appl. Catal. B 320 (2023), 121928.

[22] S. Adhikari, D.-H. Kim, Heterojunction C_3N_4/MoO_3 microcomposite for highly efficient photocatalytic oxidation of Rhodamine B, Appl. Surf. Sci. 511 (2020), 145595.

[23] A. Kumar, K. Sharma, M. Thakur, D. Pathania, A. Sharma, Fabrication of high visible light active LaFeO3/Cl-g-C3N4/RGO heterojunction for solar assisted photodegradation of aceclofenac, J. Environ. Chem. Eng. 10 (2022), 108098.

[24] J. Meyer, P.R. Kidambi, B.C. Bayer, C. Weijtens, A. Kuhn, A. Centeno, A. Pesquera, A. Zurutuza, J. Robertson, S. Hofmann, Metal oxide induced charge transfer doping and band alignment of graphene electrodes for efficient organic light emitting diodes, Sci. Rep. 4 (2014) 5380.

[25] L. Huang, H. Xu, R. Zhang, X. Cheng, J. Xia, Y. Xu, H. Li, Synthesis and characterization of g-C_3N_4/MoO_3 photocatalyst with improved visible-light photoactivity, Appl. Surf. Sci. 283 (2013) 25–32.

[26] Z. Wang, W. Wang, L. Zhang, D. Jiang, Surface oxygen vacancies on Co_3O_4 mediated catalytic formaldehyde oxidation at room temperature, Catal. Sci. Technol. 6 (2016) 3845–3853.

[27] P. Niu, L. Zhang, G. Liu, H.-M. Cheng, Graphene-like carbon nitride nanosheets for improved photocatalytic activities, Adv. Funct. Mater. 22 (2012) 4763–4770.

[28] S. Zhang, Y. Liu, R. Ma, D. Jia, T. Wen, Y. Ai, G. Zhao, F. Fang, B. Hu, X. Wang, Molybdenum (VI)-oxo clusters incorporation activates g-C3N4 with simultaneously regulating charge transfer and reaction centers for boosting photocatalytic performance, Adv. Funct. Mater. 32 (2022) 2204175.

[29] R.S. Datta, F. Haque, M. Mohiuddin, B.J. Carey, N. Syed, A. Zavabeti, B. Zhang, H. Khan, K.J. Berean, J.Z. Ou, N. Mahmood, T. Daeneke, K. Kalantar-zadeh, Highly active two dimensional α-MoO_{3-x} for the electrocatalytic hydrogen evolution reaction, J. Mater. Chem. 5 (2017) 24223–24231.

[30] S. Sun, C. Li, Z. Sun, J. Wang, X. Wang, H. Ding, In-situ design of efficient hydroxylated SiO_2/g-C_3N_4 composite photocatalyst: synergistic effect of compounding and surface hydroxylation, Chem. Eng. J. 416 (2021), 129107.

[31] J. Huang, B. Wang, Z. Hao, Z. Zhou, Y. Qu, Boosting charge separation and broadening NIR light response over defected WO_3 quantum dots coupled g-C_3N_4 nanosheets for photocatalytic degrading antibiotics, Chem. Eng. J. 416 (2021), 129109.

[32] H. Li, S. Gan, H. Wang, D. Han, L. Niu, Intercorrelated Superhybrid of AgBr Supported on Graphitic-C_3N_4-Decorated Nitrogen-Doped Graphene: high engineering photocatalytic activities for water purification and CO_2 reduction, Adv. Mater. 27 (2015) 6906–6913.

[33] C. Du, B. Yan, Z. Lin, G. Yang, Enhanced carrier separation and increased electron density in 2D heavily N-doped ZnIn2S4 for photocatalytic hydrogen production, J. Mater. Chem. A 8 (2020) 207–217.

[34] Y. Iima, D. Kuzuhara, Z.-L. Xue, S. Akimoto, H. Yamada, K. Tominaga, Time-resolved fluorescence spectroscopy study of excited state dynamics of alkyl- and benzo-substituted triphyrin (2.1.1), Phys. Chem. Chem. Phys. 16 (2014) 13129–13135.

[35] M. Jourshabani, B.-K. Lee, Unmasking the role of an amorphous/amorphous interface and a crystalline/amorphous interface in the transition of charge carriers on the CN/SiO_2/WO_3 photocatalyst, ACS Appl. Mater. Interfaces (2021).

[36] J. Hong, X. Xia, Y. Wang, R. Xu, Mesoporous carbon nitride with in situ sulfur doping for enhanced photocatalytic hydrogen evolution from water under visible light, J. Mater. Chem. 22 (2012) 15006–15012.

[37] A. Beyhaqi, Q. Zeng, S. Chang, M. Wang, S.M. Taghi Azimi, C. Hu, Construction of g-C_3N_4/WO_3/MoS_2 ternary nanocomposite with enhanced charge separation and collection for efficient wastewater treatment under visible light, Chemosphere 247 (2020), 125784.

[38] S. Li, Y. Tang, M. Wang, J. Kang, C. Jin, J. Liu, Z. Li, J. Zhu, NiO/g-C_3N_4 2D/2D heterojunction catalyst as efficient peroxymonosulfate activators toward tetracycline degradation: characterization, performance and mechanism, J. Alloy. Compd. 880 (2021), 160547.

[39] Y. Liu, C. Tang, M. Cheng, M. Chen, S. Chen, L. Lei, Y. Chen, H. Yi, Y. Fu, L. Li, polyoxometalate@metal–organic framework composites as effective photocatalysts, ACS Catal. 11 (2021) 13374–13396.

[40] C. Yan, Y. Guo, P. Wang, L. Rao, X. Ji, Y. Guo, Improved photoremoval performance of boron carbon nitride–pyromellitic dianhydride composite toward tetracycline and Cr(vi) by itself to change the solution pH, New J. Chem. 44 (2020) 11105–11124.